

Understanding Capacity Fading of MgH₂ Conversion-Type Anode via Structural Morphology Changes and Electrochemical Impedance

Abdelouahab El kharbachi,^{,§,‡} Yang Hu,^{‡,‡} Magnus H. Sørby,[§] Per Erik Vullum,[⊥]
Jan Petter Mæhlen,[§] Helmer Fjellvåg,[†] and Bjørn C. Hauback[§]*

[§] Institute for Energy Technology, P.O. Box 40, NO-2027 Kjeller, Norway

[†] Centre for Materials Science and Nanotechnology (SMN), University of Oslo, P.O. Box 1126
Blindern, NO-0318 Oslo, Norway

[⊥] SINTEF Materials and Chemistry, P.O. Box 4760 Sluppen, NO-7465 Trondheim, Norway

ABSTRACT

Previous studies have demonstrated that MgH₂ is a promising conversion-type anode toward Li with high capacity (2037 mAh/g) and low discharge/charge overpotential-hysteresis. A major challenge is the capacity loss after few cycles. To improve the understanding of the complex conversion mechanism at the electrode/electrolyte interface and of its possible evolution, a systematic investigation of the morphology–property relation is undertaken. A multitude of MgH₂ materials are obtained by mechanical milling using different devices, milling conditions and time intervals. Upon cycling, the performance of the assembled batteries is strongly dependent on the quality of the prepared MgH₂ powders. Electrochemical discharge/charge profiles ($\text{MgH}_2 \xrightarrow{\leftarrow} 2\text{LiH} + \text{Mg}$) are discussed according to the changes in microstructure and morphology revealed by powder X-ray diffraction and transmission electron microscopy. For all electrode composites, the loss of the capacity occurs typically during delithiation in agreement with a kinetically limited process namely of LiH “detachment”. Electrochemical impedance spectroscopy is meaningfully carried out using the representative tape-casted electrodes in Li/MgH₂ cells to monitor the evolution of resistance components; in particular the formation of SEI-like layer as function of particle size, state of charge and cycle number.

1. INTRODUCTION

The Li-ion battery (LIB) is a well-established technology for electrical energy storage. Thorough search of active materials has resulted in a limited set of recognized compounds which can satisfy the selection criteria regarding energy density, costs, safety and lifetime. Current anodes in LIBs are based on the concept of intercalation which has an inherent limitation of maximum one lithium atom stored per interstitial site.^{1,2} On the other hand, lithiation by means of alloying mechanisms requires the formation of multiphases (intermediate phases) leading to large activation energies and enormous volume expansions.^{3,4} The other possibility of the interaction of lithium with the host-electrode is the conversion reaction.⁵⁻⁷ Conversion-type anodes can offer new possibilities regarding their high capacity and constitute chemistries which are in the initial stage of development along the emergence of novel active materials (metal hydrides, metal oxides, complex hydrides, MnSn and many metals) for LIB technologies and beyond.^{5,8-13} More recently, a new family of transition-metal carbodiimides M-NCN (M=Fe, Mn, Zn, Cr) has been reported to undergo a conversion-type reaction during cycling with a capacity retention after hundreds of cycles of more than 600 and 400 mAh/g (C-rate C/5) in Li and Na-ion batteries respectively.¹⁴ Metal hydride-based anodes are particularly interesting owing to their high capacity and low volume expansion.¹⁵ It has been demonstrated that MgH₂ can be a candidate for conversion-type anode for LIBs.⁸ In fact, this material features high theoretical capacity 2037 mAh/g compared to graphite-anode 372 mAh/g, and low discharge-charge polarization being considered as an indicator of lifespan.^{16,17} All these vital properties, fall into line of application of hydride materials in the future electric vehicle's batteries. However, its application as anode is still a challenge owing to capacity fading after several cycles.¹⁶ MgH₂ can interact with 2Li by undergoing a conversion reaction leading to the formation of 2LiH and Mg.

At low cycling rate (C/100), MgH₂ can exchange up to 2.9Li-equivalents during the first discharge with two plateaus at 0.44 V ($\Delta x \approx 1.8\text{Li}$) and 0.095 V, the later step being attributed to the formation of the *hcp* Mg-rich and *bcc* Li-rich Mg-Li solid solutions.^{8,16} The delithiation of the Li₃Mg₇ phase has been found to be reversible under hydrogen pressure (2 MPa) at high temperatures (200°C), which may be of interest for LIB MgH₂-based anodes.¹⁸ However, the formation of these solid solutions can be avoided by restraining the discharge by capacity limit or voltage cut-off. The poor electric conductivity of MgH₂ has to be considered. Even in the presence of carbon black, this material loses its charge capacity after one discharge. The conductivity during re-charge is challenged by the insulating character of LiH. The volume variation, about 85% expansion of the electrode upon discharge, can easily lead to contact issues and loss of conductivity.¹⁹ This process is also expected to be followed by electrode surface area variation (~2-3 times) which can affect the applied current densities per surface unit.^{19,20} Previous studies have shown that the electrochemical performance depends on electrode morphology.^{16,21} In this context, the electrode preparation (tapes or pressed pellets with^{22,23} or without Ni foam²⁴) is crucial for the assessment of the cycling performance and possible *in-situ* characterization of the electrode properties using electrochemical impedance spectroscopy (EIS), as opposed to the common *post-mortem* analysis in which the surface properties of the electrodes may change during the different transfer stages.^{16,25,26} Hence, design of representative electrodes with homogenous morphology, and thus avoiding high resistance mechanically pressed pellets,^{22,24} is highly desirable to obtain consistent information on the electrochemical performance and the interfacial evolution up cycling.

The present work aims at understanding the different issues related to down capacity and complex mechanistic behavior of MgH₂-based anodes (tapes ~26 μm) during cycling by

comparing the electrodes with different microstructural properties. Samples with different particle size and microstructure were obtained by mechanical ball-milling in various conditions, including cryomilling, and at different milling times. The electrode materials were characterized using powder X-ray diffraction (PXRD), scanning and transmission electron microscopy (SEM/TEM), electrochemical cycling and EIS analysis. Insights into the limited reversibility of the MgH₂-based anodes are presented and discussed, emphasizing the importance of the *in-situ* EIS analysis of the assembled battery cells.

2. EXPERIMENTAL DETAILS

2.1. Materials Preparation

MgH₂ was purchased from Alpha-Aesar (98% purity). The MgH₂ powders were ball-milled under Ar and reactive atmosphere (50 bar H₂) using a Fritsch Pulverisette 6 planetary ball-mill with stainless steel vials and balls (ball-to-powder ratio 40:1, rotation speed 400 rpm). Milling under Ar was also performed with a Spex 8000 mixer/mill in steel vials and balls with a ball-to-powder ratio 8:1 and at liquid nitrogen temperature with a Spex 6750 Freezer mill. The latter consists of a cylindrical vial with end pieces and a cylindrical impactor made of stainless steel. The mass ratio between the impactor and the powder was 16:1. The cryomilling was carried out for different times between 15–135 min while room temperature (*RT*) milling was performed for periods between ½ h and 24 h. The milled MgH₂ powders were further mixed with carbon black for an additional 1 h milling using Spex mixer to improve the electronic conductivity. Table 1 presents the different MgH₂ samples. The detailed procedure for the preparation of the electrode tapes (~26µm thick) is described elsewhere.²¹ All sample handling was performed in a MBraun® glove box under Ar atmosphere (H₂O and O₂ < 0.1 ppm). The electrolyte 1M LiPF₆ in 1:1

ethylene carbonate/diethylene carbonate (LP30, BASF) was used without any additives and showed no reaction with the hydride.

2.2. Analysis and Characterization Tools

A home-made battery cell consisting of a stainless-steel outer casing and inner parts in titanium was used for cycling. The cell was loaded with the active material in the glove box, then covered by a separator layer (Whatman[®]) soaked in 80 μ l of the selected electrolyte, before the lithium foil was placed on top. The cells were cycled at 30°C between 0.2–2.5 V (C-rate C/20) using an Arbin Battery cycler (Arbin Instruments[®]). The voltage cut-off at 0.2 V was applied for all the cells to avoid formation of Mg-Li solid solutions at lower voltage.⁸

EIS measurements were performed on MH5, MH10 and MH24 (Table 1) using Bio-Logic[®] VSP multichannel potentiostat. Impedance was obtained for the initial cells after assembling and for the fully charged cells (2.5 V) after each cycle (C-rate C/20). An AC amplitude of 2 mV was applied over a frequency range from 200 kHz to 20 mHz. A more thorough study was carried out on sample MH24 up to 50 cycles: The as-assembled cell was discharged/charged in the voltage range 0.2–2.5 V and the impedance was obtained at both fully charged (2.5 V) and fully discharged (0.2 V) states for each cycle after 10 min float-voltage.

Synchrotron radiation powder X-ray diffraction (SR-PXD) patterns were obtained at the Swiss-Norwegian Beamlines (SNBL, BM01), ESRF, Grenoble with a Pilatus2M 2-dimensional detector and a wavelength of 0.777873 Å. The samples were contained in 0.5 mm boronglass capillaries that were rotated 90 degrees during the 30 second exposure. The sample-detector distance was 345.97 mm. 1D data were obtained by integration of the 2D diffraction patterns with the program Bubble.²⁷ Crystallite sizes were obtained with the Scherrer equation from the

positions and FWHM (Full Width at Half Maximum) of the diffraction peaks. The width of the Bragg peaks was corrected for the instrumental contribution using LaB₆ standard. The microstrain contribution to the broadening was disregarded as it remains at a minimum level after long-time milling.²⁸ TEM was performed with a double Cs corrected JEOL coldFEG ARM200CF, operated at 200 kV. A Centurio large solid angle (0.98 srad) detector was used for X-ray energy dispersive spectroscopy (EDS) analysis and a Quantum ER GIF (Gatan imaging system) was used for electron energy loss spectroscopy (EELS).

Table 1. Designation of the tested samples according to the milling times, devices and ambient conditions.

planetary mill			spex mill	cryomill	
time, h	RT, H ₂	RT, Ar	RT, Ar	time, min	liquid N ₂ , Ar
5	MH5	MA5	SA5	75	MN75
10	MH10	MA10	SA10	115	MN115
24	MH24	MA24	SA24	135	MN135

3. RESULTS AND DISCUSSION

3.1. Microstructural Characterization and Battery Tests

Mechanical grinding is an effective method for particle size reduction and provoking morphological changes which can lead to lowered activation energy and creation of vacant sites at the surface of the particles and along the grain boundaries.²⁹ Figure 1 shows the SR-PXD patterns of the as-received and MgH₂ powders ball-milled under different conditions for different durations. All Bragg peaks for the *tetra*-MgH₂ phase are well indexed with small amounts of

metallic Mg in the as-received powder. This latter phase is decreasing gradually by increased milling times in addition to a significant broadening of the Bragg peaks. For the samples milled under H₂ (Figure 1a), elemental Mg disappears after 2½h of milling. For all samples the high-pressure *ortho*-MgH₂ phase appears in accordance with earlier reports.²⁹⁻³³ Lower content of *ortho*-MgH₂ is observed in the sample that was planetary milled under Ar (Figure 1b) compared to the sample milled under H₂ (Figure 1a). The SR-PXD patterns (Figure 1c) from the samples milled in Spex mixer were comparable to the data from planetary milling under Ar atmosphere; except a small amount of Mg still remains. The milling of materials at cryogenic temperatures can prevent recrystallization/aggregation and consequently, lead to the formation of nano-sized particles. In fact, the cryomilled MgH₂ powders are less ductile and the fracturing impacts are expected to be the dominating process leading to gradual decrease of the particles size without subsequent grains welding.³⁴ The corresponding SR-PXD patterns (Figure 1d) show also significant presence of Mg and less *ortho*-MgH₂ during cryomilling up to 135 min. Furthermore, this milling process leads clearly to broader Bragg peaks compared to similar powders milled under Ar. This may be an indication of a nanocrystallinity.^{21,35}

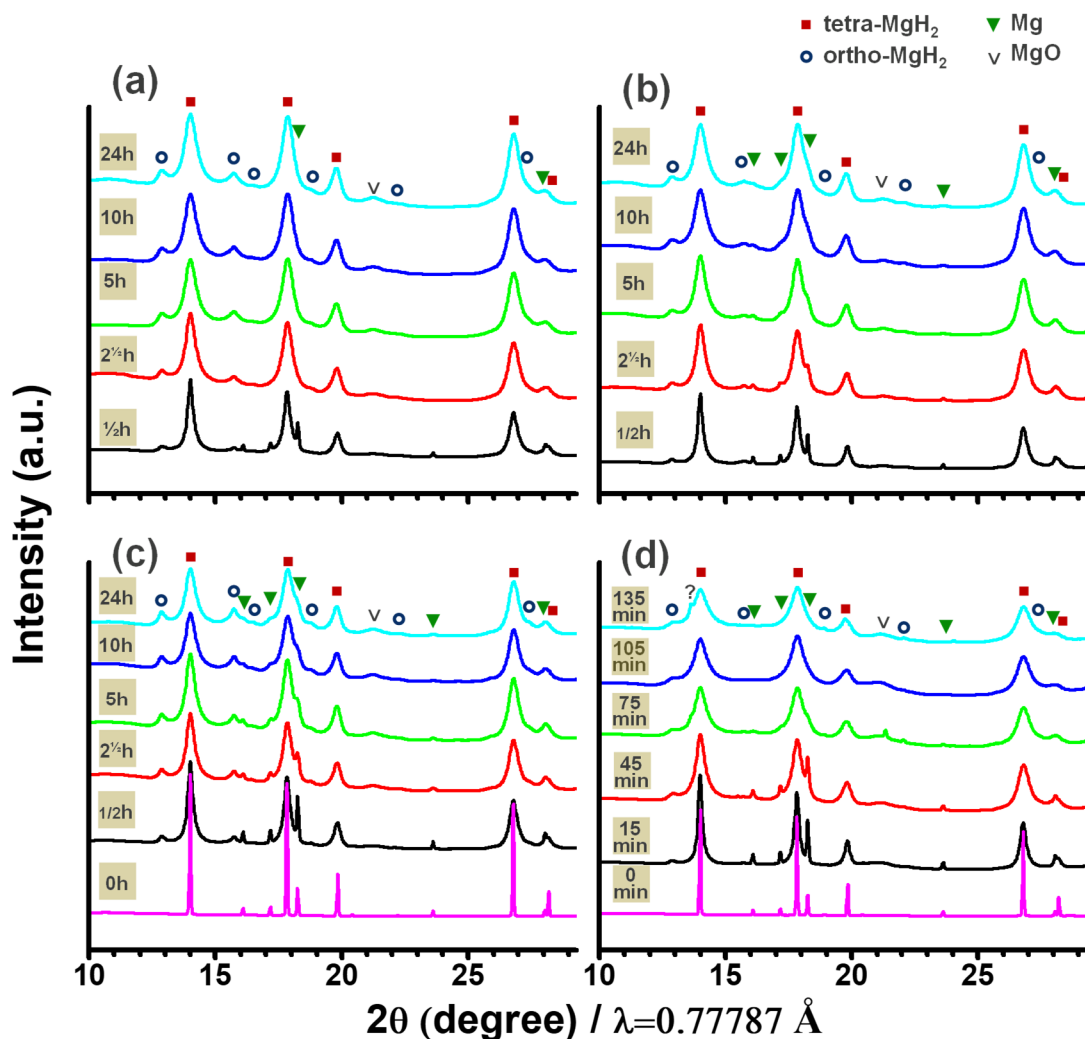


Figure 1. SR-PXD patterns of the ball-milled MgH_2 at different time intervals using planetary ball-milling (a) under H_2 and (b) Ar atmosphere, (c) Spex ball-milling and (d) cryomilling. For comparison, the as-received MgH_2 is shown in (c) and (d).

The electrochemical battery tests for the 3 first cycles of anodes prepared for the MgH_2 milled for the longest times, i.e. MH24, MA24, SA24 and MN135 in Table 1, are presented in Figure 2. In the 1st cycle, all the samples show a partially reversible process with variable yields. It can be noticed that the overpotential-hysteresis, around the working potential ~ 0.45 V, is also slightly different from one sample to another. The MH24 sample shows higher reversible capacity yield

compared to MA24 during the first cycle (49% and 37%, respectively) and flat (dis)charge plateaus with lower overpotential (Figure 2a, b). SEM images (not shown) of these two samples indicates less agglomerated particles under H₂ milling (MH24) than under Ar (MA24). In addition, the latter sample shows broader Bragg peaks of MgO, present as small particles or thin films, which may prone to block the processes at the interfaces. The discharge/charge electrochemical profiles of the SA24 sample milled with Spex (Figure 2c) do not show any significantly improved performance compared to MH24. However, both MgH₂ samples milled for 24h under Ar atmosphere, using either planetary or Spex mills, show comparable performances.

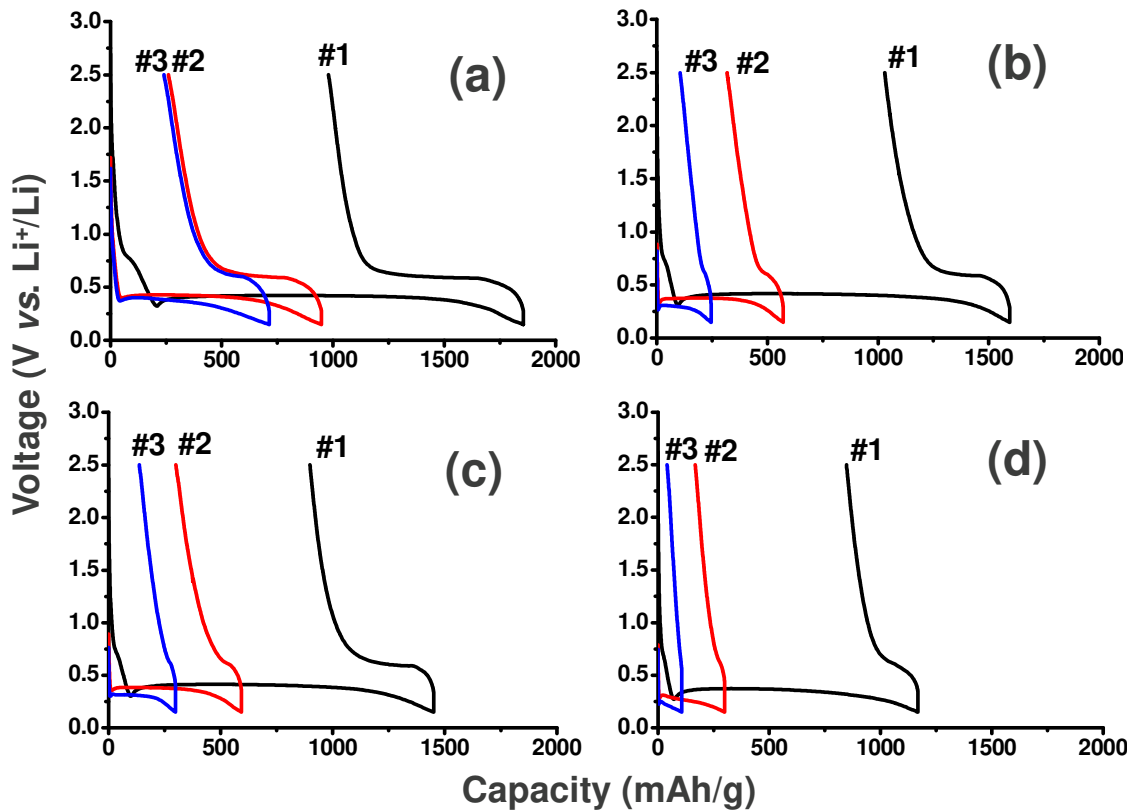


Figure 2. Galvanostatic cycling (C/20) of the 24h milled samples, (a) MH24, (b) MA24 and (c) SA24 and comparison to cryomilled (d) MN135 sample.

Despite the foreseen nanocrystallinity, the sample milled at liquid N₂ temperature shows the lowest initial discharge capacity (1150 mAh/g or 1.1Li equivalent). Only 25% of this capacity is reversible during the first cycle and the material shows an abrupt capacity loss during the 2nd/3rd cycles. Possible surface contamination of the sample with liquid N₂ cannot be ruled out, owing to under-pressure in the milling vial when Ar is liquefied. Besides, all the tested samples in Figure 2 show a rapid decrease of the reversible capacity during the 3 first cycles and become inactive after more or less 10 cycles. An origin of the discharge capacity difference between the samples milled under H₂ and Ar atmosphere (MH24 and MA24) is the variable presence of elemental Mg and *ortho*-MgH₂ with respect to *tetra*-MgH₂. This may have an effect on the total capacity and electronic properties. In fact, compared to *tetra*-MgH₂ with band gap 5.6 eV, *ortho*-MgH₂ exhibits a slightly lower band gap energy of 5.3 eV.³⁶

For the MH24-based electrode, 91% of the theoretical capacity is reached in discharge (1850 mAh/g) with a significant reversible capacity (~900 mAh/g) for the first cycle. Note that the loss of the capacity occurs typically only during the charge process. This means that almost all MgH₂ that is formed during charging, is completely converted into LiH/Mg in the consecutive discharge. However, the opposite is not the case as some of the formed LiH/Mg will not convert back to MgH₂. Obviously, the composition and morphology of the electrode are modified during each cycle; meaning this can result in accumulation of inactive LiH/Mg. Based on the amount of exchanged Li, the final composition of MH24 electrode, excluding additives, after 3 full cycles at C/20 (Figure 2a) likely consists of the three phases MgH₂/LiH/Mg in the proportions ~1:6:3 (mol. fraction). As demonstrated in our previous study,²¹ the reversible capacity of MgH₂-based anodes is significantly influenced by the kinetic rates. The charge process is much more affected

than the discharge and the reversible capacity is actually significantly higher for higher rates (C/2) than for lower ones (C/20). This suggests that the discharged state interacts readily with the electrolyte than MgH_2 does, and that the resulting aging process is kinetically limited. The enhanced performances with the MH24 electrode are still poor. Despite that, we aimed at better understanding of the chemistry and obscure mechanistic issues behind this anode material through modulated particle size using ball-milling. The following discussion will focus on the materials planetary milled under H_2 as these show better capacity and cyclability than the samples milled under other conditions.

Let us clarify on how the cycling performances are affected by the size of the particles. Three samples planetary milled under H_2 (i.e. MH5, MH10 and MH24) were selected. Figure 3 shows the particle size distribution determined from TEM for these 3 samples which seems to follow a unimodal trend with at least 75% of the particles < 300 nm. Only the sample MH5 shows the presence of particles > 1 μm , which account for around 5% of the particles in this sample. While MH10 contains 75% of the particles below 200 nm, MH24 shows more significant presence of particles lower than 100 nm. Some morphology data for the MH5, MH10 and MH24 samples are given in Figure 3 as an inset table. The coherence length calculated based on the FWHM used in the Scherrer equation gives a much smaller size (ca. 7 nm) than the particle size determined from TEM. Hence, the powder particles observed in the TEM images cannot be "perfect" single crystals. They either have to be polycrystalline and/or contain a large number of defects.

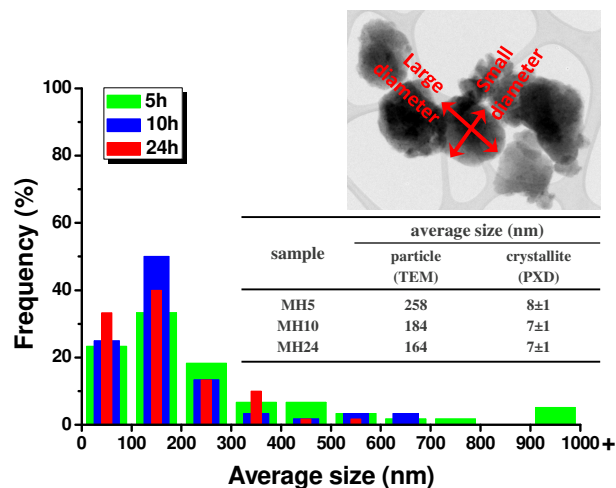


Figure 3. Particle size distribution for the 3 electrochemically analyzed MgH₂ samples: MH5, MH10 and MH24. In-set: TEM example for the estimation of the size of a single particle (statistics being based on a population of 60 particles) and table of the obtained structural morphology data of these samples.

The discharge/charge profiles of these samples are shown in Figure 4. It can be noticed an increase of the discharge capacity as well as the reversible capacity upon increased milling time and consequently reduced particle size, benefiting from larger active area of the electrode i.e. reduced ion diffusion pathways and better electronic connectivity. The sample milled for short times (MH5) shows similar discharge/charge behavior compared to the one obtained during the 2nd cycle of the corresponding 24h milled sample in Figure 2a. This point can raise the question if the particles re-agglomerate during cycling.

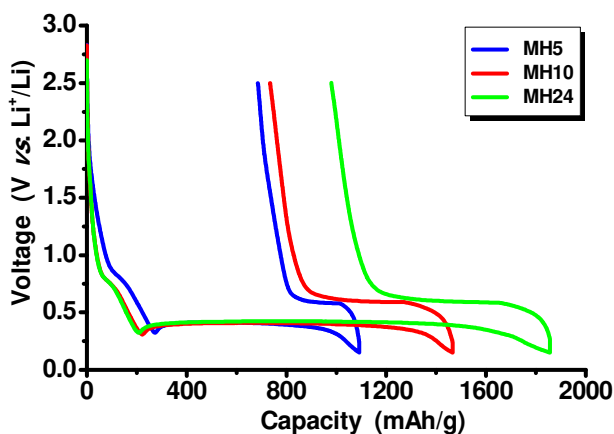


Figure 4. Comparison of the effect of the milling time on the electrochemical cycling (1 cycle, C/20) according to the ambient atmosphere under H₂ atmosphere.

Further TEM investigations have been carried out for these samples milled under H₂ atmosphere before and after the addition of battery components (carbon black, binder, electrolyte) and cycling in a Li-ion half-cell (Figure 5). As milled samples (MH5, MH10 and MH24) show significantly reduced particle size even though some coarse particles in the micron range are still present. Agglomerations of such particles with size between 200-500 nm can be observed as mentioned above (Figure 3). TEM analysis of 10 times cycled MH5/MH10/MH24 samples is displayed in Figure 5 (right side). The cycled samples showed a better stability in the electron beam compared to the as-milled powders. The scattering domains look heterogeneously dispersed for grain and particle size for the three samples. Remarkably, no significant morphological differences can be detected between the three samples after cycling. The formed particles are probably in the nanometer scale requiring the use of high resolution.

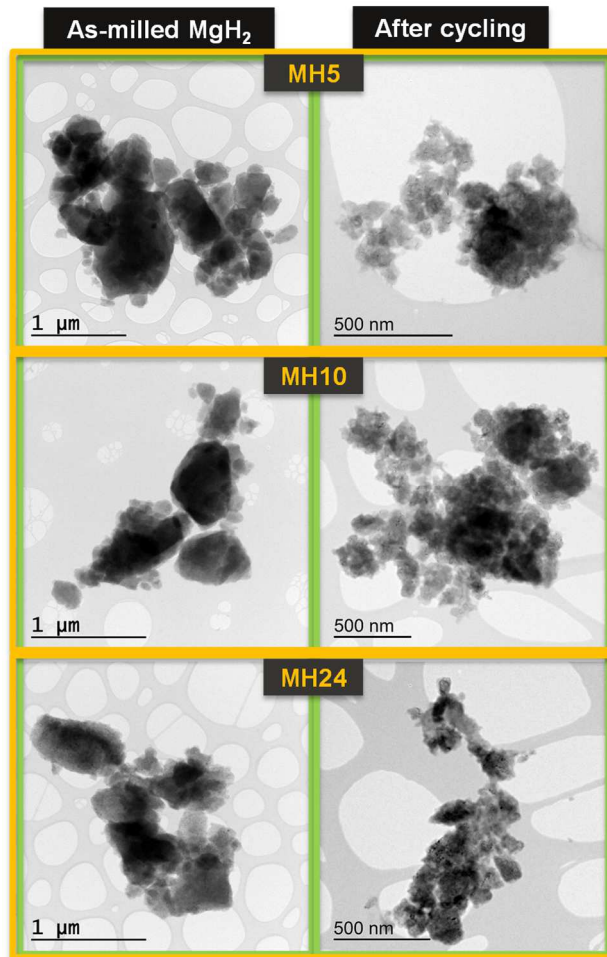


Figure 5. Bright field TEM micrographs of ball-milled MgH_2 powders MH5, MH10 and MH24 under H_2 atmosphere (a) before electrode formulation and (b) after cycling in a battery cell.

Figure 6a shows a high resolution (HR) TEM image of the 10 times cycled MH5 sample in which nanoscopic crystals can be observed together with carbon black. High angle annular dark field (HAADF) STEM imaging combined with EELS and EDS were used to map the different elements surrounding the Mg-based entities (Figure 6b, c). The quantification of the elements reveals the presence of binder/electrolyte residue (LiPF_6 in carbonate solvent) and uniform distribution of carbon and oxygen in the sample.

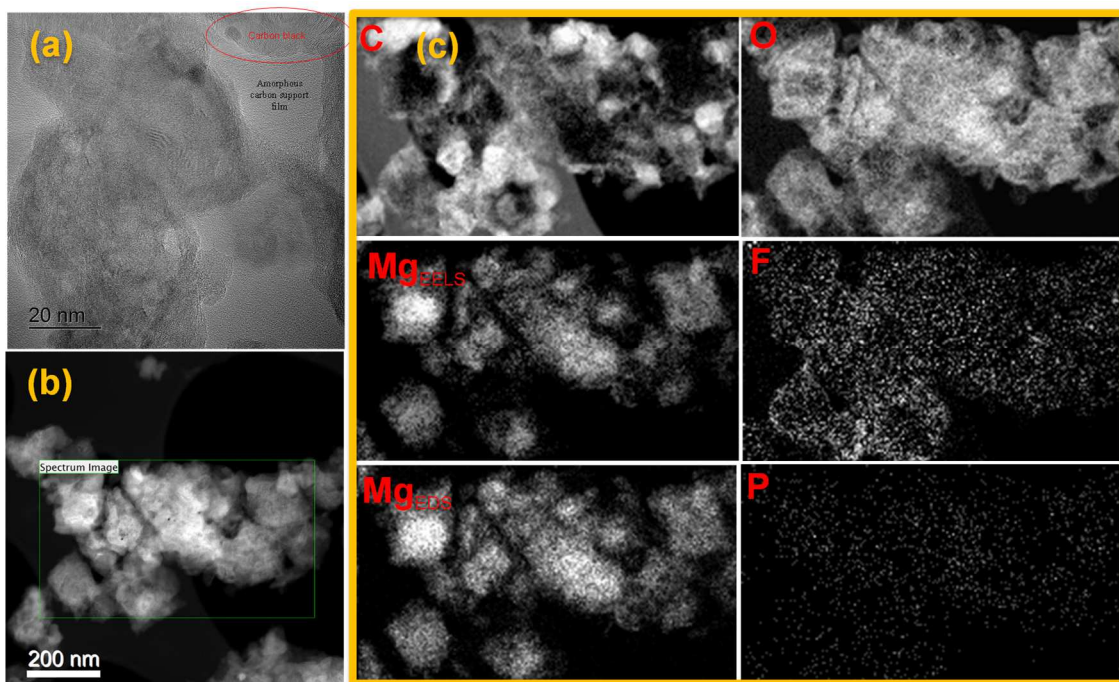


Figure 6. Electron micrographs of the electrode MH5 after cycling (a) High resolution bright field TEM and (b) HAADF STEM images. (c) The upper 4 element maps are from EELS. The lower 2 element maps are from the simultaneously acquired EDS. Some of the measured carbon comes from the TEM grid.

The HAADF STEM image (Figure S1a in Supplementary Information) and the corresponding EEL spectra (Figure S1b) of the MH10 cycled 10 times show the H *K*-peak from H anions in all areas containing Mg, thus confirming the presence of MgH_2 since positively charged H in e.g. $\text{Mg}(\text{OH})_2$ would not yield such a signal. In fact, the hydrogen *K*-peak (red plot in Figure S1b) at ca. 10 eV is very strong at the Mg-rich particles. The various features/peaks located in the region 15-25 eV are the bulk plasmon peaks which vary in energy and shape depending on the material. On the other hand, the presence of abundant LiF suggests the loss of Li mostly by interaction with the electrolyte (weaker P-F bond compared to C-F bond in the binder). It can be assumed

that this case differs from the commonly observed minor interaction of lithium with the electrolyte at the surface of graphite anode during intercalation,^{37,38} as a consequence of the more complex conversion mechanism involving the three-phase system $\text{MgH}_2\text{-Mg-LiH}$. The HAADF STEM image (Figure S2a) of the MH24-based anode after cycling reveals the same morphology of the electrode powders as shown for MH5 image in Figure 6. Additionally, the lithium map shows an interesting feature regarding the close distribution of Mg and Li-based entities (Figure S2b), such as fluoride, hydride, oxide and/or lithium carbonates.⁶ Their comprehensive chemical nature is beyond the scope of this study.

3.2. EIS *versus* Morphology, State of Charge and Cycle Number

The prepared electrode-tapes have appreciably different loading masses despite having roughly the same thickness (ca. 26 μm) and diameter (\O 15 mm). Hence, normalization by mass is necessary in order to understand the surface phenomena observed by EIS. Figure 7 shows the impedance spectra of MH5, MH10 and MH24 obtained for the initial state and the fully charged states at 2.5 V after 1st and 3rd cycles, exhibiting a similar impedance feature. At high-to-medium frequency range (> 56 Hz), the impedance spectra consist of depressed semicircles followed by inclined lines (tail) which can be associated with Warburg-type solid state diffusion (low-frequency domain < 56 Hz). A decrease of the overall impedance, reflected by the shrinking of the semicircles, has been observed in all three cells from the initial state to the fully charged state (2.5 V) after 1st and 3rd cycles. An activation process of the electrode composites, such as the formation of a solid electrolyte interphase (SEI) on the surface of carbon black and MgH_2 material resulting from minor decomposition of the electrolyte, could take place as observed in non lithiated conversion-type anodes.^{6,39,40}

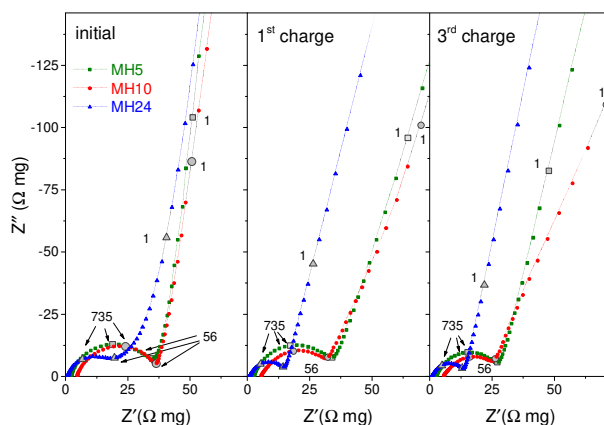


Figure 7. Impedance spectra of MH5, MH10 and MH24 based cells at the initial states, and the 1st and 3rd fully charged states (2.5 V), respectively. Impedance is normalized by the loading mass of MgH₂.

MH24 electrode exhibits considerably smaller high-to-medium semicircle (lowest resistance ~ 19 Ω.mg) compared to MH5 and MH10 (resistances close to 38 Ω.mg). This is undoubtedly due to the decrease of particle size (large electrode surface) after 24h of ball milling, which gives rise to reduced surface polarization and a better electronic connectivity in electrode composites, in agreement with the highest 1st cycle discharge capacity (Figure 4). This observation is however valid even after further cycling owing to reduced active surface as a consequence of the change in the composition of the electrode as notified above for MH24.

Extended EIS analysis was performed up to 50 cycles (C/20) for the MH24-based anode, for both fully charged (2.5 V) and discharged (0.2 V) states, as shown in Figure 8. At fully charged state (2.5 V), including the initial state of as-assembled cell (open symbol in Figure 8a), the impedance spectra consist of a depressed semicircle in the high-frequency region and an inclined

line in the low-frequency domain. While being discharged to 0.2 V (Figure 8b), the high-frequency semicircle exhibits moderate potential dependence (Figure S3) suggesting that it mainly reflects the resistance for Li^+ ion migration through the SEI-like surface films and the film capacitance. On the other hand, at discharged state a new depressed flat semicircle appears in the middle-frequency region from the 1st cycle and increases drastically for the first 3 cycles., which can be ascribed to the charge-transfer (CT) resistance and interfacial double-layer capacitance. Originally, the impedance of CT process is comparatively small probably due to better interparticle contacts with a time constant merged into the high-frequency SEI contribution. The drastic increase of medium-frequency resistance at discharged state is probably due to a slower kinetics caused by the insulating LiH layer on the particles surface. At low frequency, the impedance behaves like an inclined line representing the solid-state diffusion as well as accumulation and depletion of Li ions, depending on the cell potential.⁴¹

Equivalent circuits shown in Figure 8 (c, d) are used to fit the measure impedance. At highest frequency, the intercept of the semicircle with the real axis (Z') is indexed to an ohmic resistance (R_s) of all cell components (electrolyte resistance, contact resistance and external cell connections). At fully charged state (2.5 V), the high-frequency semicircle is ascribed to a combination of dominating SEI-like surface layer ($R_{\text{SEI}}/C_{\text{SEI}}$) and the overlapped charge-transfer ($R_{\text{ct}}/C_{\text{dl}}$) process, which are better distinguishable at discharged state (0.2 V). Therefore, the fitted R_{ct} at 2,5 V needs further confirmation. The inclined line in the low-frequency region is related to the solid-state diffusion of Li ions (Z_w) in the electrode particles or along the particle surface, and a steep slope close to 90 ° shows a more capacitive behavior associated with Li ions accumulation and insertion capacitance (C_{int}).⁶ For simplicity, only C_{int} is considered for the low-frequency inclined line at fully charged (2.5 V) state (Figure 8c), and only Z_w for the low-

frequency impedance at fully discharged state (0.2 V).⁶ It is worth noting that the separation of the SEI and CT contributions at the fully charged state is not straightforward, probably due to close time constants of these two processes. At discharged state, the original small R_{ct} might benefit from the good electronic contacts at the surface of Cu-casted electrode tapes along with the formation of metallic Mg. However, the increase of charge-transfer resistance is pronounced and irreversible, especially after few cycles. Here constant phase elements (CPE) are used to represent the capacitive elements to reflect the porosity and composite nature of the electrode.

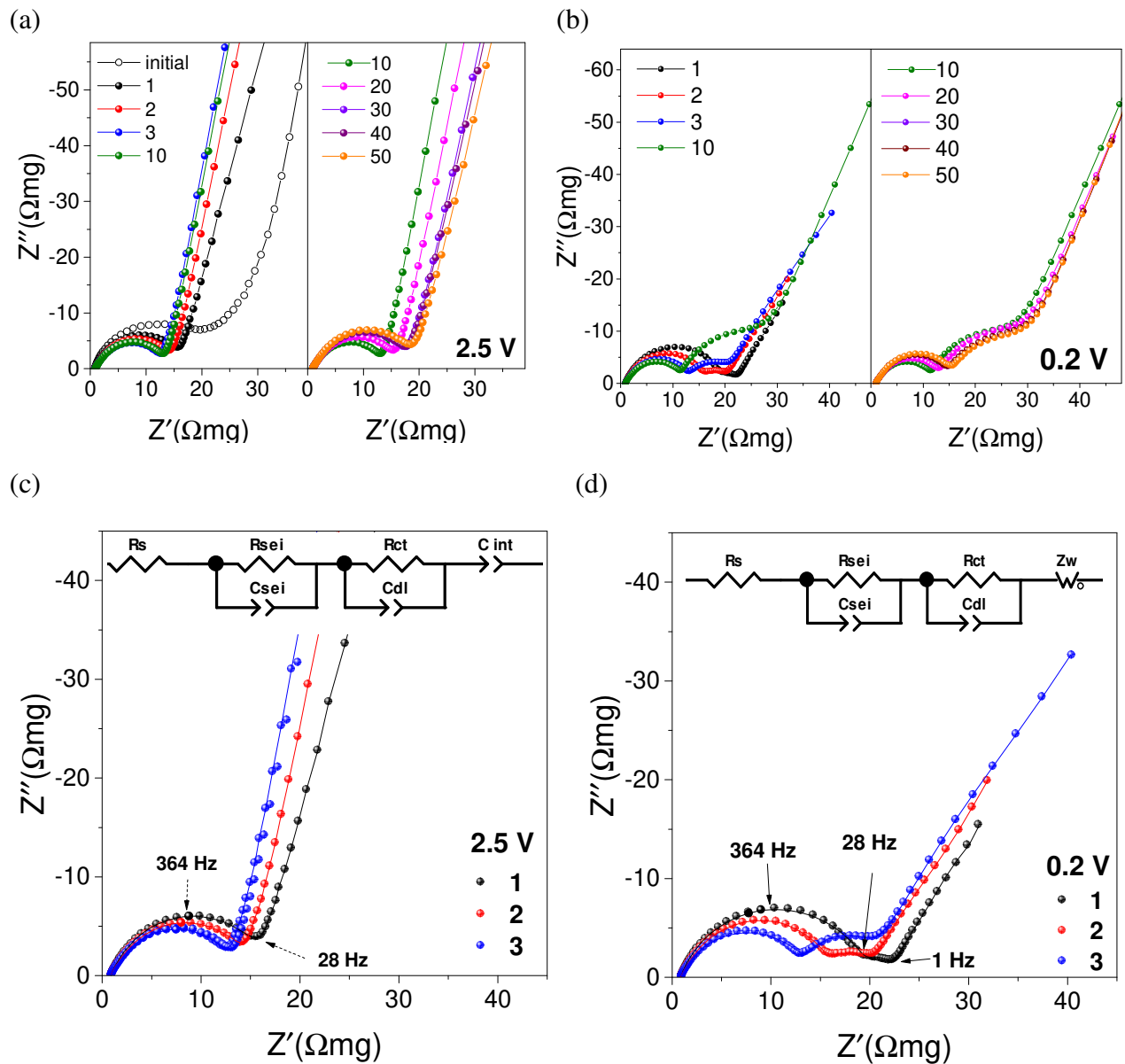


Figure 8. Impedance spectra of MH24 obtained from initial state to 50th discharge-charge cycle at (a) fully charged (2.5 V) and (b) fully discharged (0.2 V) states. (c, d) The corresponding examples of fitting using an equivalent circuit model for the first 3 cycles.

Variation of R_s , R_{SEI} , and R_{ct} as a function of the cycle number from initial to 50th cycle are shown in Figure 9. At both charged (2.5 V) and discharged (0.2 V) states, the ohmic resistance

R_s is low and only increases slightly with the cycling. This indicates a stable connectivity of cell components and as expected a stable composition and ionic conductivity of the electrolyte.

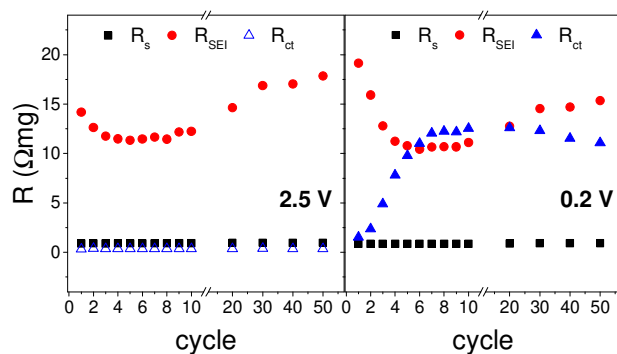


Figure 9. Variation of R_s (black), R_{SEI} (red) and R_{ct} (blue open: 2.5 V, blue solid: 0.2 V) as a function of cycle number extracted for MH24 in cycles 1–10, 20, 30, 40 and 50 at charged (2.5 V) and discharged (0.2 V) states.

On the contrary, both R_{SEI} and R_{ct} exhibit notable changes with continuous cycling. It is worth noting that R_{SEI} remains almost constant at fully charged (2.5 V) and discharged (0.2 V) states for the same cycle, though a slight difference can be seen which agree with a transient aging effect. However, a decrease in R_{SEI} from 19 Ω .mg down to 10 Ω .mg is observed from the initial state to 6th cycle. This could result from the considerable surface reduction and pulverization of the electrode upon cycling,¹⁶ as observed by TEM (Figure 5). In the extended cycles, R_{SEI} increases gradually from 10th cycle up to 50th, probably due to the growth of thicker SEI-like layer, along with electrode unravelling. An opposite evolution is observed for R_{ct} at fully discharged state, which demonstrates a continuous increase during cycling. For the first 10

cycles, R_{ct} increases drastically even the electrode particles are smaller. Hereby we can assume that during the first 10 cycles, the electrode pulverization is accompanied by the irreversible formation of the electronically insulating LiH phase and its detachment from the main electrode. Besides, it seems that a stable interface (SEI-like layer) cannot be formed during the first 10 cycles, probably due to the above mentioned changes in the electrode and the resulting continuous Li-rich SEI growth.

4. SUMMARY AND CONCLUSIONS

The study of the mechanistic properties of MgH_2 anodes has been undertaken in carbonate-based liquid electrolyte. A series of MgH_2 samples were prepared by utilizing 4 milling modes and conditions and the formulated electrodes were electrochemically tested in a Li-ion half-cell. The loss of the capacity occurs typically during re-charge process for all samples, generating inactive LiH/Mg entities. The sample milled under H_2 using planetary ball-milling shows the best cycling performance with particles of reduced size (150 nm). The particles formed after cycling were in the nano-range as observed by HR-TEM, of which Mg and Li-based entities are in close distribution. The EIS results show that the formation of an interface (SEI-like layer) occurs as soon as the electrode is in contact with the electrolyte, and R_{SEI} seems to decrease upon cycling (1-10 cycles) and depends on the electrode initial particle size. The ohmic resistance remains stable upon cycling; no significant electrolyte depletion is observed. For the same morphology electrode, the resistance R_{ct} observed at the discharged state increases with cycling, in agreement with the formation of inactive phases along with the electrode surface change during the first 10 cycles. The by-products of the irreversible reaction have a clear effect on the impedance of both discharged and charged cells, due to migration of the inactive species into the

electrolyte. In addition, the persistent rise of charge-transfer resistance agrees with continuously polarized electrodes and the growth of thick SEI layer upon cycling. Though Li-based species are still present in the *ex-situ* characterized electrodes; their interaction as “LiH detachment” from the electrolyte needs to be clarified (isolation, solubility, side reaction *etc*). However, we have demonstrated here the possibility to study the conversion mechanism of MgH₂ anodes using EIS, where particles are deposited on dendritic Cu avoiding high resistance of the mechanically pressed pellets reported so far.

ASSOCIATED CONTENT

Supporting Information. Figure S1. Electron micrographs of the electrode MH10 after cycling: HAADF STEM imaging with the corresponding EEL spectra of the defined spectrum image. Figure S2. HAADF-STEM image with the reconstructed Z^2 -scaled contrast maps of the MH24 electrode. Figure S3. Comparison of impedance obtained at 2.5 V and 0.2 V states in the charge-discharge cycle 1, 3, and 10. Solid red lines represent the fitting results using equivalent circuits in the main text (Figures 8c, d). The following files (PDF) are available free of charge.

AUTHOR INFORMATION

Corresponding Author

*E-mail: abdele@ife.no.

Author Contributions

The manuscript was written through contributions of all authors. All authors have given approval to the final version of the manuscript. ‡ These authors contributed equally.

Notes

Any additional relevant notes should be placed here.

ACKNOWLEDGMENT

This work is financially supported by Research Council of Norway under the program EnergiX, Project no. 244054, LiMBAT - "Metal hydrides for Li-ion battery anodes". AE thanks Dr S. Deledda for advice on the milling conditions used to prepare the multitude MgH₂ electrodes. We acknowledge the skillful assistance from the staff of SNBL at ESRF, Grenoble, France. The TEM work was carried out on NORTEM infrastructure, Grant 197405, TEM Gemini Centre, Norwegian University of Science and Technology (NTNU), Norway.

REFERENCES

- (1) Armand, M.; Tarascon, J. M. Building better batteries. *Nature* **2008**, *451*, 652-657.
- (2) Larcher, D.; Tarascon, J. M. Towards greener and more sustainable batteries for electrical energy storage. *Nat. Chem.* **2015**, *7*, 19-29.
- (3) Yang, J.; Winter, M.; Besenhard, J. O. Small particle size multiphase Li-alloy anodes for lithium-ionbatteries. *Solid State Ionics* **1996**, *90*, 281-287.
- (4) McDowell, M. T.; Lee, S. W.; Nix, W. D.; Cui, Y. 25th Anniversary Article: Understanding

the Lithiation of Silicon and Other Alloying Anodes for Lithium-Ion Batteries. *Adv. Mater.* **2013**, *25*, 4966-4985.

(5) Poizot, P.; Laruelle, S.; Grugéon, S.; Dupont, L.; Tarascon, J. M. Nano-sized transition-metal oxides as negative-electrode materials for lithium-ion batteries. *Nature* **2000**, *407*, 496-499.

(6) Marino, C.; Darwiche, A.; Dupré, N.; Wilhelm, H. A.; Lestriez, B.; Martinez, H.; Dedryvère, R.; Zhang, W.; Ghamouss, F.; Lemordant, D., et al. Study of the Electrode/Electrolyte Interface on Cycling of a Conversion Type Electrode Material in Li Batteries. *J. Phys. Chem. C* **2013**, *117*, 19302-19313.

(7) Boyanov, S.; Bernardi, J.; Gillot, F.; Dupont, L.; Womes, M.; Tarascon, J. M.; Monconduit, L.; Doublet, M. L. FeP: Another Attractive Anode for the Li-Ion Battery Enlisting a Reversible Two-Step Insertion/Conversion Process. *Chem. Mater.* **2006**, *18*, 3531-3538.

(8) Oumellal, Y.; Rougier, A.; Nazri, G. A.; Tarascon, J. M.; Aymard, L. Metal hydrides for lithium-ion batteries. *Nat. Mater.* **2008**, *7*, 916-921.

(9) Binotto, G.; Larcher, D.; Prakash, A. S.; Herrera Urbina, R.; Hegde, M. S.; Tarascon, J. M. Synthesis, Characterization, and Li-Electrochemical Performance of Highly Porous Co₃O₄ Powders. *Chem. Mater.* **2007**, *19*, 3032-3040.

(10) Teprovich, J. A.; Zhang, J.; Colón-Mercado, H.; Cuevas, F.; Peters, B.; Greenway, S.; Zidan, R.; Latroche, M. Li-Driven Electrochemical Conversion Reaction of AlH₃, LiAlH₄, and NaAlH₄. *J. Phys. Chem. C* **2015**, *119*, 4666-4674.

(11) Hamelet, S.; Tzedakis, T.; Leriche, J.-B.; Sailer, S.; Larcher, D.; Taberna, P.-L.; Simon, P.; Tarascon, J.-M. Non-Aqueous Li-Based Redox Flow Batteries. *J. Electrochem. Soc.* **2012**, *159*, A1360-A1367.

(12) Meggiolaro, D.; Farina, L.; Silvestri, L.; Panero, S.; Brutti, S.; Reale, P. Lightweight

Borohydrides Electro-Activity in Lithium Cells. *Energies* **2016**, *9*, 238.

(13) Dalverny, A. L.; Filhol, J. S.; Doublet, M. L. Interface electrochemistry in conversion materials for Li-ion batteries. *J. Mater. Chem.* **2011**, *21*, 10134-10142.

(14) Sougrati, M. T.; Darwiche, A.; Liu, X.; Mahmoud, A.; Hermann, R. P.; Jouen, S.; Monconduit, L.; Dronskowski, R.; Stievano, L. Transition-Metal Carbodiimides as Molecular Negative Electrode Materials for Lithium- and Sodium-Ion Batteries with Excellent Cycling Properties. *Angew. Chem. Int. Ed.* **2016**, *55*, 5090-5095.

(15) Sartori, S.; Cuevas, F.; Latroche, M. Metal hydrides used as negative electrode materials for Li-ion batteries. *Appl. Phys. A* **2016**, *122*, 135.

(16) Brutti, S.; Mulas, G.; Piciollo, E.; Panero, S.; Reale, P. Magnesium hydride as a high capacity negative electrode for lithium ion batteries. *J. Mater. Chem.* **2012**, *22*, 14531-14537.

(17) Meggiolaro, D.; Gigli, G.; Paolone, A.; Reale, P.; Doublet, M. L.; Brutti, S. Origin of the Voltage Hysteresis of MgH₂ Electrodes in Lithium Batteries. *J. Phys. Chem. C* **2015**, *119*, 17044-17052.

(18) Kumar, S.; Singh, A.; Kojima, Y.; Dey, G. K. Tailoring the Thermodynamics and Kinetics of Mg-Li Alloy for a MgH₂-Based Anode for Lithium-Ion Batteries. *Energy Technology* **2017**, *5*, 1546-1551.

(19) Aymard, L.; Oumellal, Y.; Bonnet, J.-P. Metal hydrides: an innovative and challenging conversion reaction anode for lithium-ion batteries. *Beilstein J. Nanotechnol.* **2015**, *6*, 1821-1839.

(20) Aboulaich, A.; Bouchet, R.; Delaizir, G.; Sez nec, V.; Tortet, L.; Morcrette, M.; Rozier, P.; Tarascon, J.-M.; Viallet, V.; Dollé, M. A New Approach to Develop Safe All-Inorganic Monolithic Li-Ion Batteries. *Adv. Energy Mater.* **2011**, *1*, 179-183.

- (21) El kharbachi, A.; Andersen, H. F.; Sørby, M. H.; Vullum, P. E.; Mæhlen, J. P.; Hauback, B. C. Morphology effects in MgH₂ anode for lithium ion batteries. *Int. J. Hydrogen Energy* **2017**, *42*, 22551-22556.
- (22) Huen, P.; Ravnsbæk, D. B. Insight into Poor Cycling Stability of MgH₂ Anodes. *J. Electrochem. Soc.* **2017**, *164*, A3138-A3143.
- (23) Yang, S.; Wang, H.; Ouyang, L.; Liu, J.; Zhu, M. Improvement in the Electrochemical Lithium Storage Performance of MgH₂. *Inorganics* **2018**, *6*, 2.
- (24) Silvestri, L.; Navarra, M. A.; Brutti, S.; Reale, P. Failure mechanism of NaAlH₄ negative electrodes in lithium cells. *Electrochim. Acta* **2017**, *253*, 218-226.
- (25) Oumellal, Y.; Zlotea, C.; Bastide, S.; Cachet-Vivier, C.; Leonel, E.; Sengmany, S.; Leroy, E.; Aymard, L.; Bonnet, J.-P.; Latroche, M. Bottom-up preparation of MgH₂ nanoparticles with enhanced cycle life stability during electrochemical conversion in Li-ion batteries. *Nanoscale* **2014**, *6*, 14459-14466.
- (26) Zaïdi, W.; Oumellal, Y.; Bonnet, J. P.; Zhang, J.; Cuevas, F.; Latroche, M.; Bobet, J. L.; Aymard, L. Carboxymethylcellulose and carboxymethylcellulose-formate as binders in MgH₂-carbon composites negative electrode for lithium-ion batteries. *J. Power Sources* **2011**, *196*, 2854-2857.
- (27) Dyadkin, V.; Pattison, P.; Dmitriev, V.; Chernyshov, D. A new multipurpose diffractometer PILATUS@SNBL. *J. Synchrotron Rad.* **2016**, *23*, 825-829.
- (28) Varin, R. A.; Czujko, T.; Wronski, Z. Particle size, grain size and γ -MgH₂ effects on the desorption properties of nanocrystalline commercial magnesium hydride processed by controlled mechanical milling. *Nanotechnology* **2006**, *17*, 3856-3865.
- (29) Schulz, R.; Huot, J.; Liang, G.; Boily, S.; Lalande, G.; Denis, M. C.; Dodelet, J. P. Recent

developments in the applications of nanocrystalline materials to hydrogen technologies. *Mat. Sci. Eng.* **1999**, *267*, 240-245.

(30) Bastide, J.-P.; Bonnetot, B.; Létouffé, J.-M.; Claudy, P. Polymorphisme de l'hydruure de magnesium sous haute pression. *Mater. Res. Bull.* **1980**, *15*, 1215-1224.

(31) Vajeeston, P.; Ravindran, P.; Hauback, B. C.; Fjellvåg, H.; Kjekshus, A.; Furuseth, S.; Hanfland, M. Structural stability and pressure-induced phase transitions in MgH₂. *Phys. Rev. B* **2006**, *73*, 224102.

(32) Selvam, P.; Viswanathan, B.; Swamy, C. S.; Srinivasan, V. Magnesium and magnesium alloy hydrides. *Int. J. Hydrogen Energy* **1986**, *11*, 169-192.

(33) Yavari, A. R.; de Castro, J. F. R.; Vaughan, G.; Heunen, G. Structural evolution and metastable phase detection in MgH₂-5%NbH nanocomposite during in-situ H-desorption in a synchrotron beam. *J. Alloys Compd.* **2003**, *353*, 246-251.

(34) Riktor, M. D.; Deledda, S.; Herrich, M.; Gutfleisch, O.; Fjellvåg, H.; Hauback, B. C. Hydride formation in ball-milled and cryomilled Mg-Fe powder mixtures. *Mater. Sci. Eng. B* **2009**, *158*, 19-25.

(35) Paskevicius, M.; Sheppard, D. A.; Buckley, C. E. Thermodynamic Changes in Mechanochemically Synthesized Magnesium Hydride Nanoparticles. *J. Am. Chem. Soc.* **2010**, *132*, 5077-5083.

(36) Moysés Araújo, C.; Ahuja, R. Electronic and optical properties of pressure induced phases of MgH₂. *J. Alloys Compd.* **2005**, *404-406*, 220-223.

(37) Xu, K. "Charge-Transfer" Process at Graphite/Electrolyte Interface and the Solvation Sheath Structure of Li⁺ in Nonaqueous Electrolytes. *J. Electrochem. Soc.* **2007**, *154*, A162-A167.

- (38) Aurbach, D. Review of selected electrode-solution interactions which determine the performance of Li and Li ion batteries. *J. Power Sources* **2000**, *89*, 206-218.
- (39) Mahmoud, A.; Chamas, M.; Lippens, P.-E. Electrochemical impedance study of the solid electrolyte interphase in MnSn₂ based anode for Li-ion batteries. *Electrochim. Acta* **2015**, *184*, 387-391.
- (40) Tesfaye, A. T.; Yücel, Y. D.; Barr, M. K. S.; Santinacci, L.; Vacandio, F.; Dumur, F.; Maria, S.; Monconduit, L.; Djenizian, T. The Electrochemical Behavior of SnSb as an Anode for Li-ion Batteries Studied by Electrochemical Impedance Spectroscopy and Electron Microscopy. *Electrochim. Acta* **2017**, *256*, 155-161.
- (41) Aurbach, D.; Levi, M. D.; Levi, E.; Teller, H.; Markovsky, B.; Salitra, G.; Heider, U.; Heider, L. Common Electroanalytical Behavior of Li Intercalation Processes into Graphite and Transition Metal Oxides. *Journal of The Electrochemical Society* **1998**, *145*, 3024-3034.

